ARTICLE IN PRESS

Nature Communications

https://doi.org/10.1038/s41467-026-71743-y

Article in Press

Spin-polarized light-emitting diodes based on CrI_3 operating without external spin injection

Received: 7 November 2025

Accepted: 31 March 2026

Chung-Chun Lu, Li-Wei Chang, Wei-Qing Li, Po-Liang Chen, Yen-Ju Lin, Kun-Hung Pan, Ching Kuo & Chang-Hua Liu

Cite this article as: Lu, C.-C., Chang, L.-W., Li, W.-Q. *et al.* Spin-polarized light-emitting diodes based on CrI_3 operating without external spin injection. *Nat Commun* (2026). https://doi.org/10.1038/s41467-026-71743-y

We are providing an unedited version of this manuscript to give early access to its findings. Before final publication, the manuscript will undergo further editing. Please note there may be errors present which affect the content, and all legal disclaimers apply.

If this paper is publishing under a Transparent Peer Review model then Peer Review reports will publish with the final article.

ARTICLE IN PRESS

© The Author(s) 2026. **Open Access** This article is licensed under a Creative Commons Attribution-NonCommercial-NoDerivatives 4.0 International License, which permits any non-commercial use, sharing, distribution and reproduction in any medium or format, as long as you give appropriate credit to the original author(s) and the source, provide a link to the Creative Commons licence, and indicate if you modified the licensed material. You do not have permission under this licence to share adapted material derived from this article or parts of it. The images or other third party material in this article are included in the article's Creative Commons licence, unless indicated otherwise in a credit line to the material. If material is not included in the article's Creative Commons licence and your intended use is not permitted by statutory regulation or exceeds the permitted use, you will need to obtain permission directly from the copyright holder. To view a copy of this licence, visit http://creativecommons.org/licenses/by-nc-nd/4.0/.

Spin-polarized light-emitting diodes based on CrI_3 operating without external spin injection

Chung-Chun Lu ≠[1], Li-Wei Chang ≠[1], Wei-Qing Li[1], Po-Liang Chen[1], Yen-Ju Lin[1, 2], Kun-Hung Pan[1], Ching Kuo[1], Chang-Hua Liu[1, 3, 4*]

≠These authors contributed equally to this work

1. Institute of Photonics Technologies, National Tsing Hua University, Hsinchu 30013, Taiwan

2. Artilux Inc., Zhubei City, Hsinchu 30288, Taiwan

3. Department of Electrical Engineering, National Tsing Hua University, Hsinchu, 30013, Taiwan

4. College of Semiconductor Research, National Tsing Hua University, Hsinchu, 30013, Taiwan

*Corresponding authors. Email: chliu@ee.nthu.edu.tw

Abstract:

Spin-polarized light-emitting diodes convert electron spin into circularly polarized light, enabling direct optical readout of spin information and applications in on-chip information processing. Previous demonstrations have largely relied on GaAs-based emitters integrated with spin injectors. These devices, however, require complex epitaxial growth, limiting integration, while high circular polarization remains difficult, demanding high-quality materials for efficient spin injection, coherent spin transport, and spin-conserving radiative recombination. Here, we report an alternative approach for spin-polarized light-emitting diodes by employing monolayer CrI_3 as the emitter, sandwiched between two graphene/hexagonal boron nitride tunneling contacts. Although these contacts inject unpolarized carriers into CrI_3, the resulting electroluminescence exhibits circular polarization, with helicity governed by the magnetic order of CrI_3. Notably, the electroluminescence degree of polarization reaches 20% and its helicity can be reversed with a low magnetic field (~0.17 T). Combined with the inherent integrability of heterostructures, this approach provides a promising platform for future on-chip spin-optoelectronics.

Introduction

Solid-state spin-polarized light-emitting diodes (spin-LEDs) have long been pursued for their ability to convert electron spin into circularly polarized light, enabling direct optical readout of spin information. Their inherent compatibility with integrated photonic circuits further broadens their potential for cryptography, reconfigurable optical interconnects, and advanced optical switches[1,2]. Typically, these solid-state spin-LEDs operate by injecting spin-polarized carriers into a bandgap semiconductor, where optical selection rules couple the non-equilibrium spin population to the circular polarization of emitted photons; reversing the external magnetic field flips the injected spin orientation, thereby switching the EL helicity[1-3]. Early realizations of this concept were achieved using GaAs-based semiconductors as the emitting layer, integrated with ferromagnetic metals, dilute magnetic semiconductors such as (Ga,Mn)As and $Be_xMn_\gamma Zn_{1-x-\gamma}Se$, or tunneling spin filters such as MgO to serve as spin injectors[1,2,4-8]. However, these approaches yield intricate multilayer heterostructures, and their fabrication requires sophisticated epitaxial growth, limiting device integrability. To overcome these challenges, recent efforts have turned to emerging two-dimensional (2D) materials as a new platform for device design. Their layered nature allows the assembly of complex heterostructures and direct integration on diverse substrates without lattice or thermal mismatch issues[9-11], opening new opportunities for spin-LED development. For instance, monolayer transition metal dichalcogenides (TMDs), with their unique spin–valley properties[12-14], have been exploited to generate circularly polarized EL through integration with spin injectors such as permalloy or (Ga,Mn)As, or via electric-double-layer transistor architectures[15-18]. More recently, 2D magnets have been implemented as spin injectors[19-22], enabling the injection of spin-polarized carriers into TMDs and the realization of fully vdW spin-LED architectures. This can be realized by using Fe_3GeTe_2 as a spin source, yielding degree of circular polarization (DOCP) ~8% at 78 K, with nonvolatile DOCP sign reversal under a low magnetic field (~0.1 T) [19]. Alternatively, trilayer CrI_3 can function as a spin-filter barrier, producing EL from TMDs with a DOCP of up to ~40%. This is achieved at 4 K under an ~2 T magnetic field, which ensures CrI_3 converts from an antiferromagnetic to a ferromagnetic state and enables efficient spin filtering. [20].

Despite these advances, most spin-LEDs reported to date rely on external spin injectors. Such architectures demand efficient injection of spin-polarized carriers, preservation of spin coherence during transport, and spin-conserving radiative recombination in the emitter. All three processes are highly sensitive to material defects and interfacial properties, which directly impact the DOCP and render device optimization nontrivial[1-3]. To move beyond the above-mentioned limitations, an attractive strategy is to employ 2D magnets directly as the light-emitting medium, exploiting the intrinsic coupling between excitons and the magnetic order to produce polarized emission. This concept has recently been validated in $NiPS_3$, where EL exhibits an ultranarrow linewidth (~1 meV) and a high degree of linear polarization, arising from excitons coupled to the underlying antiferromagnetic order[21,22].

In this context, the magnetic 2D semiconductor CrI_3 emerges as a promising platform for realizing injector-free spin-LEDs. Identified as the first experimentally demonstrated 2D ferromagnet, monolayer CrI_3 exhibits a Curie temperature of ~45 K and an out-of-plane easy axis of magnetization, while few-layer CrI_3 adopts a layered type-A antiferromagnetic ground state[23-25]. Additionally, unlike most bandgap semiconductors where light emission arises from Wannier–Mott excitons, CrI_3 emits via intra-atomic *d*–*d* transitions within the Cr^{3+} ions, correlated with the ligand field of the surrounding halides. This localized emission is intrinsically linked to the magnetic order, resulting in circularly polarized photoluminescence (PL) whose helicity reflects the orientation of the magnetization[26-28]. Provided that EL from CrI_3 can be realized, these features could in principle allow the emission helicity to be controlled solely via tuning the magnetic state of the CrI_3 layer, without relying on external spin injectors. However, this concept has yet to be experimentally demonstrated, even though it is conceptually straightforward.

Here, we report the experimental realization of spin-LEDs based on vdW heterostructures, with monolayer CrI_3 serving as the light-emitting layer. Helicity-resolved EL measurements show that, under an upward (downward) out-of-plane magnetic field, the emission exhibits stronger σ^- (σ^+) circular polarization, with the EL DOCP reaching -20% (20%). Moreover, the EL DOCP reverses in a nearly square hysteresis as the magnetic field direction is swept. This behaviour closely matches the magnetic hysteresis measured by reflective magnetic circular dichroism (RMCD) and magneto-PL, providing clear evidence that the EL helicity is directly governed by the intrinsic magnetic order of CrI_3. These findings establish a new approach for designing spin LEDs and, combined with the integrability of vdW heterostructures, pave the way for future spin-optoelectronic devices enabling on-chip information processing.

Results

Device structure and characterization of 2D CrI_3

Figure 1a,b presents a schematic and an optical micrograph of the investigated vdW spin-LED heterostructures. Details of the material preparation and device fabrication are provided in the Methods section. In this device, monolayer CrI_3 serves as the light-emitting layer, encapsulated between two tunneling contacts composed of graphene and hexagonal boron nitride (hBN). Graphene acts as a transparent and highly conductive electrode[29,30], while bilayer hBN flakes function as tunneling barriers, allowing electrons and holes to efficiently tunnel from graphene into CrI_3, where they persist long enough to undergo radiative recombination under an applied bias voltage[31-33]. The emissive capability of CrI_3 is verified by PL measurement (Fig. 1c), which exhibits an emission peak centered at 1.14 μm. The relatively broad linewidth, with a full width at half maximum (FWHM) of ~190 nm, reflects coupling between electronic excitation and lattice vibrations, in agreement with previous reports on CrI_3-based optical emission[26].

To probe the intrinsic magnetic properties of CrI_3, we performed polar RMCD measurements (see Methods) as a function of an externally applied magnetic field oriented perpendicular to the sample plane (i.e., in the Faraday geometry). Unless otherwise specified, all RMCD and subsequent optoelectronic measurements were conducted at 30 K. As shown in Fig. 1d, the resulting hysteresis loop displays a square-like shape with a coercive field of approximately 0.17 T and a finite RMCD signal at zero field, confirming that the CrI_3 used here exhibits ferromagnetic ordering with an out-of-plane easy magnetization axis characteristic of an Ising-type magnet. The fact that only a single hysteresis loop appears near zero field further indicates that the used CrI_3 is monolayer, consistent with the known layer-dependent magnetic behaviour[5,20].

Next, we perform magneto-PL measurements (see Methods) on the used monolayer CrI_3 to resolve the effect of applying magnetic field on its PL helicity. Figure 2a presents the helicity-resolved PL spectra under a magnetic field of 0.6 T, where an apparent intensity contrast between the σ^+ and σ^- components is observed, with σ^- emission stronger. The PL DOCP, defined as $(I_+ - I_-)/(I_+ + I_-)$ with I_+ and I_- denoting the peak intensities of measured σ^+ and σ^- emission, respectively, reaches around -20%. This helicity contrast remains even as the magnetic field is reduced from 0.6 T to zero (Fig. 2b). When the field is reversed to −0.6 T, the σ^+ emission becomes dominant, yielding DOCP around 20%, and this helicity state is retained as the field returns to zero (Fig. 2c-d). These results reveal a direct coupling between PL helicity and the magnetic order of CrI_3, because magnetic fields of 0.6 T (-0.6T) are sufficient to fully align the magnetization in the out-of-plane upward (downward) orientation. Moreover, as the magnetic field is swept, the PL DOCP shows non-volatile behaviour, reversing its sign at approximately ±0.17 T (Supplementary Section 1), matching the ferromagnetic hysteresis observed in the RMCD measurement (Fig. 1d).

EL generation from graphene/hBN/CrI_3/hBN/graphene heterostructures

With these fundamental characterizations, we then examine the electrical behaviour and the feasibility of generating EL in our proposed graphene/hBN/CrI_3/hBN/graphene heterostructures. Figure 3a shows the I–V_b characteristics measured by applying a bias (V_b) across the graphene electrodes, with the bottom electrode grounded. The nearly symmetric tunneling diode-like response under both bias polarities indicates the absence of band tilting across the heterostructure at equilibrium (Fig. 3b). When a bias is applied, it induces a vertical electric field that tilts the energy bands, while simultaneously shifting the Fermi levels of the two graphene electrodes due to the quantum capacitance effect (Fig. 3c)[34]. Once the Fermi levels align with the electronic states of CrI_3, carriers begin to tunnel efficiently through the atomically thin hBN barriers, causing the turn-on of the tunneling diode and initiating EL emission (Fig. 3d–e).

Notably, at low injected current (~few hundreds nA), the EL peak wavelength coincides with the PL peak (~1.14 µm), and the EL spatial map shows that emission is confined to the CrI_3 region (Supplementary Section 2), confirming that the observed EL originates from intra-atomic *d*–*d* transitions within CrI_3. Moreover, we note that this tunneling device structure can sustain high injected currents up to 50 µA (corresponding to a current density of 250 A/cm^2 for the graphene/CrI_3/graphene overlapped area of 20 µm^2) while continuing to emit light. However, at higher bias, the EL intensity increases sublinearly with current (Fig. 3f, lower panel), and the emission peak exhibits a slight redshift from 1.14 µm to 1.17 µm (Fig. 3f, upper panel), accompanied by a noticeable broadening of the EL linewidth (Fig. 3d–e). The sublinear scaling of EL intensity at high bias can be attributed to a combination of device- and material-related effects. That is, the high bias creates a strong vertical electric field that enhances direct carrier tunneling between the graphene electrodes, reducing the fraction of carriers that recombine radiatively within CrI_3 [31-33], while strong carrier injection can also introduce nonradiative recombination pathways through exciton−exciton annihilation[35], further limiting the EL efficiency. To clarify the origin of the bias-induced spectral changes, we first consider the possible contribution of Joule heating. Finite-element simulations reveal that increasing the current to 50 µA raises the device temperature by ~6 K, from 30 K to approximately 36 K (Supplementary Section 3). However, temperature-dependent PL measurements on monolayer CrI_3 (Supplementary Section 4) indicate that this modest temperature increase produces negligible spectral changes, suggesting that additional mechanisms may contribute. Indeed, recent studies have shown that excitonic emission in CrI_3 can be described by exciton-polaron, Frenkel-exciton, or self-trapped-exciton models[28,36,37]. Within these frameworks, an increasing exciton population enhances phonon sidebands and lattice distortions, leading to emission redshift and linewidth broadening, potentially accounting for the bias-dependent spectral evolution.

Evidence for graphene/hBN/CrI_3/hBN/graphene heterostructures as spin-LEDs

Following this, we demonstrate the potential of CrI_3-based heterostructures for spin-LED applications. In pursuit of this, an out-of-plane magnetic field was applied onto heterostructures in the Faraday geometry to probe the influence of magnetic order on EL helicity. As shown in Fig. 4a, helicity-resolved EL spectra measured at an injected current of 0.5 μA reveal a dominant σ^--polarized emission under a 0.6 T out-of-plane field. The resulting EL DOCP of -19.5%, comparable to the PL DOCP shown in Fig. 2, even though the graphene electrodes inject unpolarized carriers. Upon reversing the magnetic field to −0.6 T at the same injection current, the emission helicity switches correspondingly, resulting in a DOCP of 19.5% (Fig. 4b). These observations indicate that this proof-of-concept vdW spin-LED can achieve polarized EL performance without external spin injection or filtering, highlighting the potential of CrI_3 for simpler spin-LED architectures and yielding DOCP values that exceed most conventional III–V and II–VI epitaxial devices (see Supplementary Section 5 for a comparison table)[1,2]. Moreover, the EL intensity and DOCP remain stable after 48 hours of continuous operation, and measurements on multiple independently fabricated CrI_3-based spin-LEDs show consistent DOCP values of 17–23%, suggesting stable operation and good device-to-device reproducibility (Supplementary Section 6).

To further verify that the observed EL helicity originates from the ferromagnetic order of CrI_3, we measured the EL DOCP at an injected current of 0.5 μA as a function of the out-of-plane magnetic field. As shown in Fig. 4c, the EL polarization exhibits a clear hysteresis loop that generally follows the RMCD hysteresis of CrI_3, suggesting a strong connection between the EL helicity and its magnetic order. But it is worth noting that the sign reversal of the EL DOCP loop occurs at approximately ±0.1 T, lower than the coercive field obtained from RMCD and magneto-PL loop experiments (~0.17 T, Fig. 1d and also see Supplementary Section 1). This difference could be partially attributed to the distinct probing characteristics of the measurements: RMCD and PL are sensitive to local magnetization at a focused spot[23], whereas EL integrates emission across the entire CrI_3 layer, effectively averaging over possible domain variations[23]. Another factor that could contribute to this discrepancy is the applied bias. It induces carrier injection, which raises the device temperature via Joule heating, and increases the chemical potential of the graphene electrodes[34], enabling carriers to be populated into higher-energy orbitals in CrI_3 and activating antiferromagnetic exchange interactions[38]. Thus, the bias-related effect could weaken the ferromagnetism of CrI_3 and could account for the sign reversal of the EL DOCP loop at lower magnetic fields (see Supplementary Section 7 for further evidence) as well as the decrease in EL DOCP from 19.5% to 2.5% with increasing injection current (Fig. 4d).

In addition to monolayer CrI_3 devices, the dependence of EL polarization on the magnetic state of CrI_3 is also evident in Gr/hBN/CrI_3/hBN/Gr heterostructures employing bilayer CrI_3 as the emitter. In this spin-LED, the EL exhibits a DOCP of approximately ±22% when the bilayer is in the ferromagnetic (↑ ↑/↓ ↓) configuration, comparable to that observed in monolayer emitters. However, the EL helicity vanishes as the external magnetic field drops to zero (see Supplementary Section 8 for magneto-EL from a spin-LED based on bilayer CrI_3), directly reflecting the layered antiferromagnetic ground state of bilayer CrI_3 (↑ ↓ or ↓ ↑)[23-25], in which each layer emits circularly polarized light of opposite helicity. Taken together, the results from EL DOCP loops and layer-dependent CrI_3 heterostructure experiments reveal a direct correlation between the magnetic order of CrI_3 and the helicity of its EL.In summary, we demonstrate a new approach to realizing spin-LEDs by employing a 2D magnet, CrI_3, as the light-emitting layer. In this architecture, polarized EL is enabled by the intrinsic magneto-excitonic coupling in CrI_3, rather than by external spin injection. This design therefore circumvents the integration of spin injectors and the intricate heterostructure engineering required to suppress spin decoherence, both of which remain major challenges for most spin-LEDs developed to date[1,2]. Building on this framework, we anticipate that higher degrees of polarization can be achieved by lowering the device operating temperature, inducing hole doping, or applying mechanical strain to CrI_3, approaches that have been shown to enhance its ferromagnetism[25,38-40]. Moreover, the electrostatic gate tunability of CrI_3 offers additional opportunities to modulate magnetic order, such as tuning ferromagnetism in monolayers or driving antiferromagnetic-to-ferromagnetic transitions in bilayers, thereby enabling gate-controlled modulation of the DOCP[25,41]. Beyond CrI_3, the approach can be extended to other emerging 2D magnets with different bandgaps, such as $CrBr_3$, whose luminescence is similarly coupled to magnetic order as in CrI_3, thereby enabling spin-LEDs operating at different emission wavelengths[42-44]. Finally, the vdW nature of our proposed spin-LEDs allows seamless integration with a variety of photonic platforms[9,45], supporting on-chip architectures where helicity control can be harnessed for advanced functionalities in optical communication, information processing, and quantum photonics[2,3].

Methods:

Fabrication of vdW heterostructures

All graphene, hBN, and CrI_3 flakes used in this work were obtained by mechanical exfoliation, and their thicknesses were identified using atomic force microscopy (AFM) and optical contrast methods following established procedures[23]. The vdW heterostructures were assembled by sequentially stacking the selected flakes through a dry transfer process[10]. The completed graphene/hBN/CrI_3/hBN/graphene stacks were transferred onto a Si/SiO_2 substrate prepatterned with two separated Ti/Au (5/50 nm) electrodes. During assembly, the top and bottom graphene layers were precisely aligned to make contact with the respective electrodes. All exfoliation and transfer processes were carried out in a nitrogen-filled glove box, where oxygen and water levels were maintained below 0.5 ppm to prevent material oxidation. After assembly, the heterostructures were wire-bonded onto a chip carrier and promptly mounted in a cryogenic system for subsequent measurements.

Optoelectronic measurements

All fabricated vdW heterostructures were wire-bonded onto chip carriers and mounted on the cold finger of a cryostat maintained at 30 K. An electromagnet surrounding the cryostat generated an out-of-plane magnetic field in the Faraday geometry for the following optoelectronic measurements. For RMCD characterization, the helicity-dependent reflectivity of the vdW heterostructures was measured using a 633 nm HeNe laser (10 μW), whose polarization state was periodically switched between right- and left-handed circular polarizations by a photoelastic modulator. The modulated beam was normally incident and focused to a ~1 μm spot on the vdW heterostructure through an aspheric lens. The reflected light retraced the same optical path and was collected by a balanced amplified photodetector. The resulting signal was then sent to a lock-in amplifier to extract the differential reflectivity between the two helicities[19,23,46].

For magneto-PL measurements, the same HeNe laser was used to excite the CrI_3 layer while an out-of-plane magnetic field was applied to the heterostructure. The emitted PL was collected by an aspheric lens and analyzed using a grating spectrometer (Andor Shamrock 500i) equipped with an Andor iDus InGaAs CCD camera. PL spectra were recorded as a function of the applied magnetic field to probe helicity-dependent emission behaviour. For both RMCD and PL measurements, the excitation power was kept low (10 μW) to minimize sample heating and degradation.

For magneto-EL measurements, the light emitted from the vdW heterostructures under applied bias was collected using the same optical setup as for PL, and helicity-resolved EL spectra were recorded as a function of the out-of-plane magnetic field to examine the correlation between the emission polarization and the magnetic order of the CrI_3 layer.

Data availability:

Source Data are provided with this paper. Relevant data supporting the key findings of this study are available within the article and the Supplementary Information file.

References:

1 Holub, M. & Bhattacharya, P. Spin-polarized light-emitting diodes and lasers. *J. Phys. D.* **40**, 179-203 (2007).
2 Zutic, I., Fabian, J. & Das Sarma, S. Spintronics: fundamentals and applications. *Rev. Mod. Phys.* **76**, 323–410 (2004).
3 Hirohata, A. *et al.* Review on spintronics: principles and device applications. *J. Magn. Magn. Mater.* **509**, 166711 (2020).
4 Ohno, Y. *et al.* Electrical spin injection in a ferromagnetic semiconductor heterostructure. *Nature* **402**, 790-792 (1999).
5 Fiederling, R. *et al.* Injection and detection of a spin-polarized current in a light-emitting diode. *Nature* **402**, 787-790 (1999).
6 Ramsteiner, A., Zhu, H. J., Schönherr, H. P. & Ploog, K. H. Electrical spin injection from Fe into GaAs at room temperature. *Physica E* **13**, 529-532 (2002).
7 Jiang, X. *et al.* Highly spin-polarized room-temperature tunnel injector for semiconductor spintronics using MgO(100). *Phys. Rev. Lett.* **94**, 056601 (2005).
8 Zarpellon, J. *et al.* Spin injection at remanence into III-V spin light-emitting diodes using (Co/Pt) ferromagnetic injectors. *Phys. Rev. B* **86**, 205314 (2012).
9 Jariwala, D., Marks, T. J. & Hersam, M. C. Mixed-dimensional van der Waals heterostructures. *Nat. Mater.* **16**, 170-181 (2017).
10 Liu, Y. *et al.* Van der Waals heterostructures and devices. *Nat. Rev. Mater.* **1**, 16042 (2016).
11 Novoselov, K. S., Mishchenko, A., Carvalho, A. & Neto, A. H. C. 2D materials and van der Waals heterostructures. *Science* **353**, aac9439 (2016).
12 Xu, X. D., Yao, W., Xiao, D. & Heinz, T. F. Spin and pseudospins in layered transition metal dichalcogenides. *Nat. Phys.* **10**, 343-350 (2014).

13 Mak, K. F., Xiao, D. & Shan, J. Light-valley interactions in 2D semiconductors. *Nat. Photon.* **12**, 451-460 (2018).

14 Mak, K. F., He, K. L., Shan, J. & Heinz, T. F. Control of valley polarization in monolayer MoS_2 by optical helicity. *Nat. Nanotech.* **7**, 494-498 (2012).

15 Ye, Y. *et al.* Electrical generation and control of the valley carriers in a monolayer transition metal dichalcogenide. *Nat. Nanotech.* **11**, 597-602 (2016).

16 Sanchez, O. L., Ovchinnikov, D., Misra, S., Allain, A. & Kis, A. Valley polarization by spin injection in a light-emitting van der Waals heterojunction. *Nano Lett.* **16**, 5792-5797 (2016).

17 Zhang, Y. J., Oka, T., Suzuki, R., Ye, J. T. & Iwasa, Y. Electrically switchable chiral light-emitting transistor. *Science* **344**, 725-728 (2014).

18 Pu, J. *et al.* A Versatile and simple approach to generate light emission in semiconductors mediated by electric double layers. *Adv. Mater.* **29**, 1606918 (2017).

19 Li, J. X. *et al.* Electric control of valley polarization in monolayer WSe_2 using a van der Waals magnet. *Nat. Nanotech.* **17**, 721-728 (2022).

20 Dang, J. C. *et al.* Electrical switching of spin-polarized light-emitting diodes based on a 2D CrI_3/hBN/WSe_2 heterostructure. *Nat. Commun.* **15**, 6799 (2024).

21 Hwangbo, K. *et al.* Highly anisotropic excitons and multiple phonon bound states in a van der Waals antiferromagnetic insulator. *Nat. Nanotech.* **16**, 655-660 (2021).

22 Lebedev, D. *et al.* Ultranarrow electroluminescence from magnetic excitons in the van der Waals antiferromagnetic semiconductor $NiPS_3$. *Nat. Commun.* **16**, 10550 (2025).

23 Huang, B. *et al.* Layer-dependent ferromagnetism in a van der Waals crystal down to the monolayer limit. *Nature* **546**, 270-273, (2017).

24 Song, T. C. *et al.* Giant tunneling magnetoresistance in spin-filter van der Waals heterostructures. *Science* **360**, 1214-1218 (2018).

25 Jiang, S. W., Li, L. Z., Wang, Z. F., Mak, K. F. & Shan, J. Controlling magnetism in 2D CrI3 by electrostatic doping. *Nat. Nanotech.* **13**, 549-553 (2018).

26 Seyler, K. L. *et al.* Ligand-field helical luminescence in a 2D ferromagnetic insulator. *Nat. Phys.* **14**, 277-281 (2018).

27 Wu, M., Li, Z. L., Cao, T. & Louie, S. G. Physical origin of giant excitonic and magneto-optical responses in two-dimensional ferromagnetic insulators. *Nat. Commun.* **10**, 2371 (2019).

28 Grzeszczyk, M. *et al.* Strongly Correlated Exciton-Magnetization System for Optical Spin Pumping in $CrBr_3$ and CrI_3. *Adv. Mater.* **35**, e202209513 (2023).

29 Mak, K. F. *et al.* Measurement of the optical conductivity of graphene. *Phys. Rev. Lett.* **101**, 196405 (2008).

30 Chang, Y. C., Liu, C. H., Liu, C. H., Zhong, Z. H. & Norris, T. B. Extracting the complex optical conductivity of mono- and bilayer graphene by ellipsometry. *Appl. Phys. Lett.* **104**, 261909 (2014).

31 Withers, F. *et al.* Light-emitting diodes by band-structure engineering in van der Waals heterostructures. *Nat. Mater.* **14**, 301-306 (2015).

32 Liu, C. H. *et al.* Nanocavity integrated van der Waals heterostructure light-emitting tunneling diode. *Nano Lett.* **17**, 200-205 (2017).

33 Withers, F. *et al.* WSe_2 light-emitting tunneling transistors with enhanced brightness at room temperature. *Nano Lett.* **15**, 8223-8228 (2015).

34 Yu, G. L. *et al.* Interaction phenomena in graphene seen through quantum capacitance. *Proc. Natl Acad. Sci. USA* **110**, 3282–3286 (2013).

35 Sridhar, S. *et al.* Ligand field exciton annihilation in bulk $CrCl_3$. *J. Chem. Phys.* **161**, 114706 (2024).

36 Li, X. F. *et al.* Ultrafast spontaneous localization of a Jahn–Teller exciton polaron in two-dimensional semiconducting CrI_3 by symmetry breaking. *Nano Lett.* **22,** 8755–8762 (2022).

37 Bai, Y. F., Wang, Y. X. & Meng, S. Ab initio self-trapped excitons. *Phys. Rev. Lett.* **133**, 046903 (2024).

38 Orozovic, M., Soskic, B. N., Picozzi, S., Sljivancanin, Z. & Stavric, S. Hole doping as an efficient route to increase the Curie temperature in monolayer CrI_3. *2D Mater.* **12**, 045025 (2025).

39 Webster, L. & Yan, J. A. Strain-tunable magnetic anisotropy in monolayer $CrCl_3$, $CrBr_3$, and CrI_3. *Phys. Rev. B* **98**, 144411 (2018).

40 Huang, B. *et al.* Emergent phenomena and proximity effects in two-dimensional magnets and heterostructures. *Nat. Mater.* **19**, 1276-1289 (2020).

41 Huang, B. *et al.* Electrical control of 2D magnetism in bilayer CrI_3. *Nat. Nanotech.* **13**, 544-548 (2018).

42 Zhang, Z. W. *et al.* Direct photoluminescence probing of ferromagnetism in monolayer two-dimensional $CrBr_3$. *Nano Lett.* **19**, 3138-3142 (2019).

43 Wang, Q. H. *et al.* The magnetic genome of two-dimensional van der Waals materials. *ACS Nano* **16**, 6960-7079 (2022).

44 Liu, S., Malik, I. A., Zhang, V. L. & Yu, T. Lightning the spin: harnessing the potential of 2D magnets in opto-Spintronics. *Adv. Mater.* **37**, 2306920 (2025).

45 Liu, C. H., Zheng, J. J., Chen, Y. Y., Fryett, T. & Majumdar, A. Van der Waals materials integrated nanophotonic devices. *Opt. Mater. Express* **9**, 384–399 (2019).

46 Sato, K. Measurement of magneto-optical Kerr effect using piezo-birefringent modulator. *Jpn J. Appl. Phys.* **20**, 2403–2409 (1981).

Acknowledgements:

C.-H.L. acknowledges support from the National Tsing Hua University (114Q2708E1) and the National Science and Technology Council (NSTC 114-2628-M-007 -002, 113-2223-E-007-008-MY3).

Author Contributions:

C.-H.L. conceived the experiments and supervised the project. C.-C.L. and L.-W.C. fabricated the vdW heterostructures, assisted by P.-L.C. C.K. and K.-H.P. C.-C.L. and L.-W.C. performed the measurements, assisted by W.-Q.L. and C.-H.L. Y.-J.L. provided numerical simulations. All authors contributed to the discussion of the data in the manuscript and Supplementary Information.

Competing Interests:

The authors declare no competing interests.

Figure Captions:

Figure 1 Device structure of the vdW heterostructure spin-LED and characterization of the CrI_3 light-emitting layer. a. Top-view schematic of the monolayer CrI_3 crystal structure and device configuration, showing vertically stacked graphene/hBN/CrI_3/hBN/graphene heterostructures. b. Optical microscope image of the vdW heterostructure spin-LED. The regions of top graphene (Gr_T), bottom graphene (Gr_B) and monolayer CrI_3 are defined by blue, red and white dashed lines, respectively. Scale bar, 10 µm. c. PL spectrum measured from the used CrI_3 flake, excited with a linearly polarized 633 nm laser at 10 μW. d. RMCD as a function of applied magnetic field on the used CrI_3 flake. Red (Black) data points denote the RMCD value when sweeping the magnetic field in the negative (positive) direction.

Figure 2 Magneto-PL of monolayer CrI_3. a–d. Polarization-resolved PL spectra for σ^- (black) and σ^+ (red) detection, recorded sequentially at the following magnetic field stages: (a) after ramping from 0 to 0.6 T; (b) after ramping down from 0.6 T to 0; (c) after ramping from 0 to −0.6 T; (d) after ramping up from −0.6 T back to 0. All spectra were excited with a linearly polarized 633 nm laser at 10 μW. In panels (a)–(d), positive and negative magnetic fields are defined as pointing outward from and inward toward the surface of monolayer CrI_3, respectively. The blue arrows indicate the magnetic field sweep direction.

Figure 3 Electrical properties, energy band diagram, and EL characteristics of vdW heterostructures. a. I–V_b characteristics of the light-emitting heterostructures measured under a bias applied across the graphene electrodes, with the bottom electrode grounded. b–c. Schematic energy band diagrams of the vdW heterostructures under (b) zero bias ($V_b = 0$) and (c) positive bias ($V_b > 0$), showing electrons and holes tunneling from the graphene electrodes into CrI_3 (blue and red arrows), and their transitions between the t_{2g} and e_g orbitals within Cr^{3+} (gray arrow) generate electroluminescence. Because of crystal-field interactions, the d orbitals of Cr^{3+} split into three lower-energy t_{2g} orbitals (d_{xy}, d_{yz}, d_{xz}) and two higher-energy e_g orbitals ($d_{x^2-y^2}$, d_{z^2}). d. EL intensity map as a function of injected current. e. Line cuts extracted from panel (d), showing representative EL spectra at different levels of injected current. The spectra exhibit several dips near 1370 nm, originating from H_2O and CH_4 absorption. f. EL peak wavelength (upper panel) and peak intensity (lower panel) versus injected current.

Figure 4 Evidence of spin-LED operation in graphene/hBN/CrI_3/hBN/graphene heterostructures.

a-b. Polarization-resolved EL spectra for σ^- (black) and σ^+ (red) detection, with the magnetic field at (a) 0.6 T and (b) -0.6 T, respectively. c. Change of the degree of EL polarization as a function of applied magnetic field. Red (black) data points denote the EL polarization measured when sweeping the magnetic field in the negative (positive) direction. In panels (a)–(c), positive and negative magnetic fields are defined as pointing outward from and inward toward the surface of the heterostructures, respectively, and the spin-LED was measured under an injected current of 0.5 μA. d. Current-dependent change in the EL DOCP, measured as the injected current was increased from 0.5 μA to 50 μA. The magnetic field was swept from –0.6 T to 0 T and then fixed at 0 T prior to the current-dependent measurement.

Editor's Summary

This study shows spin-LEDs based on a 2D magnet that emit circularly polarized light with helicity controlled by its magnetic order without the need for external spin injectors, offering a simple, integrable platform for future spin-optoelectronics.

Peer review information: *Nature Communications* thanks Yunqiu Kelly Luo who co-reviewed with Thow Min Cham; Thow Min Cham and the other anonymous reviewer(s) for their contribution to the peer review of this work. A peer review file is available.

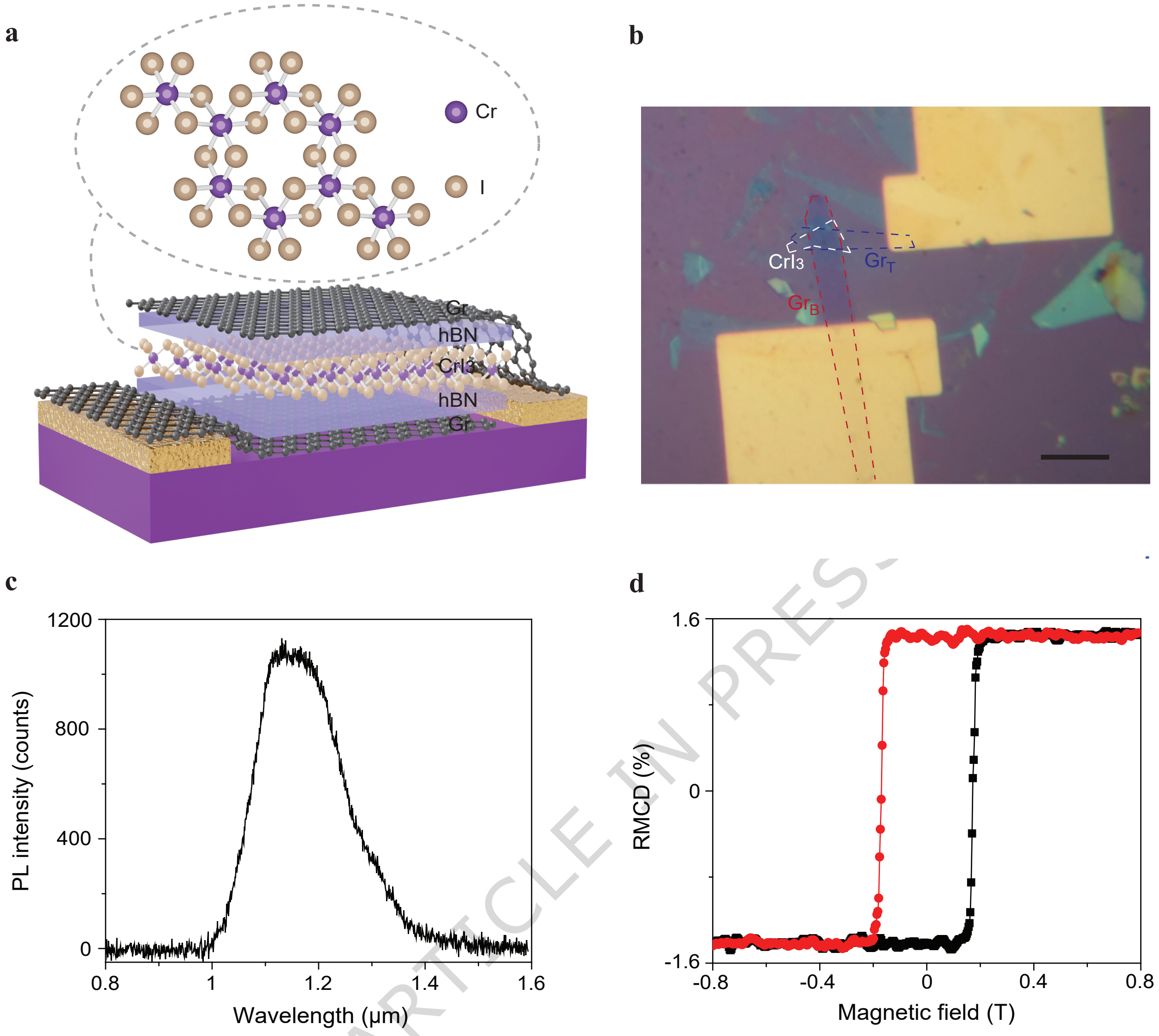
a
Cr
I
Gr
hBN
CrI3
hBN
Gr
b
CrI3
Gr_T
Gr_B
c
PL intensity (counts)
1200
800
400
0
0.8
1
1.2
1.4
1.6
Wavelength (μm)
d
RMCD (%)
1.6
0
-1.6
-0.8
-0.4
0
0.4
0.8
Magnetic field (T)

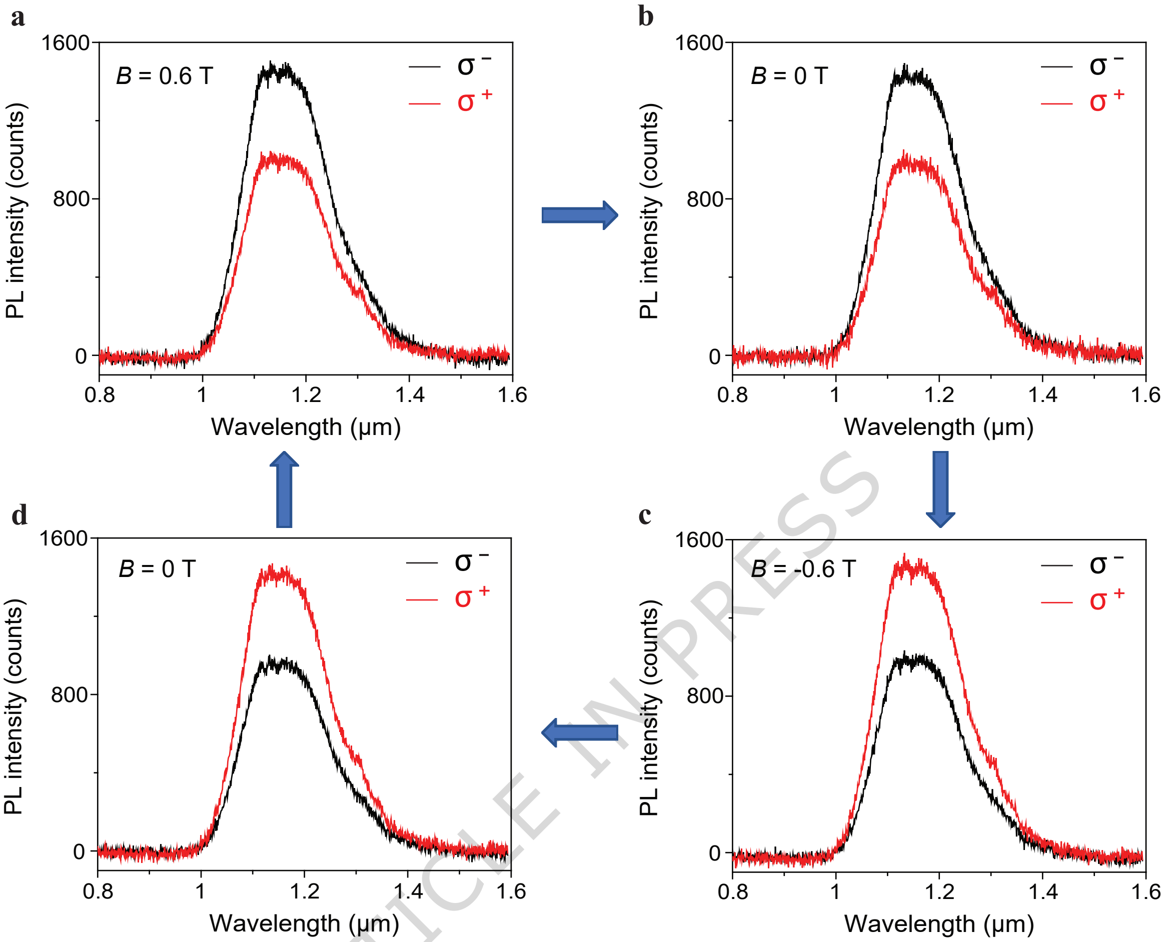
a
b
c
d
B = 0.6 T
B = 0 T
B = -0.6 T
B = 0 T
σ⁻
σ⁺
PL intensity (counts)
0
800
1600
Wavelength (μm)
0.8
1
1.2
1.4
1.6

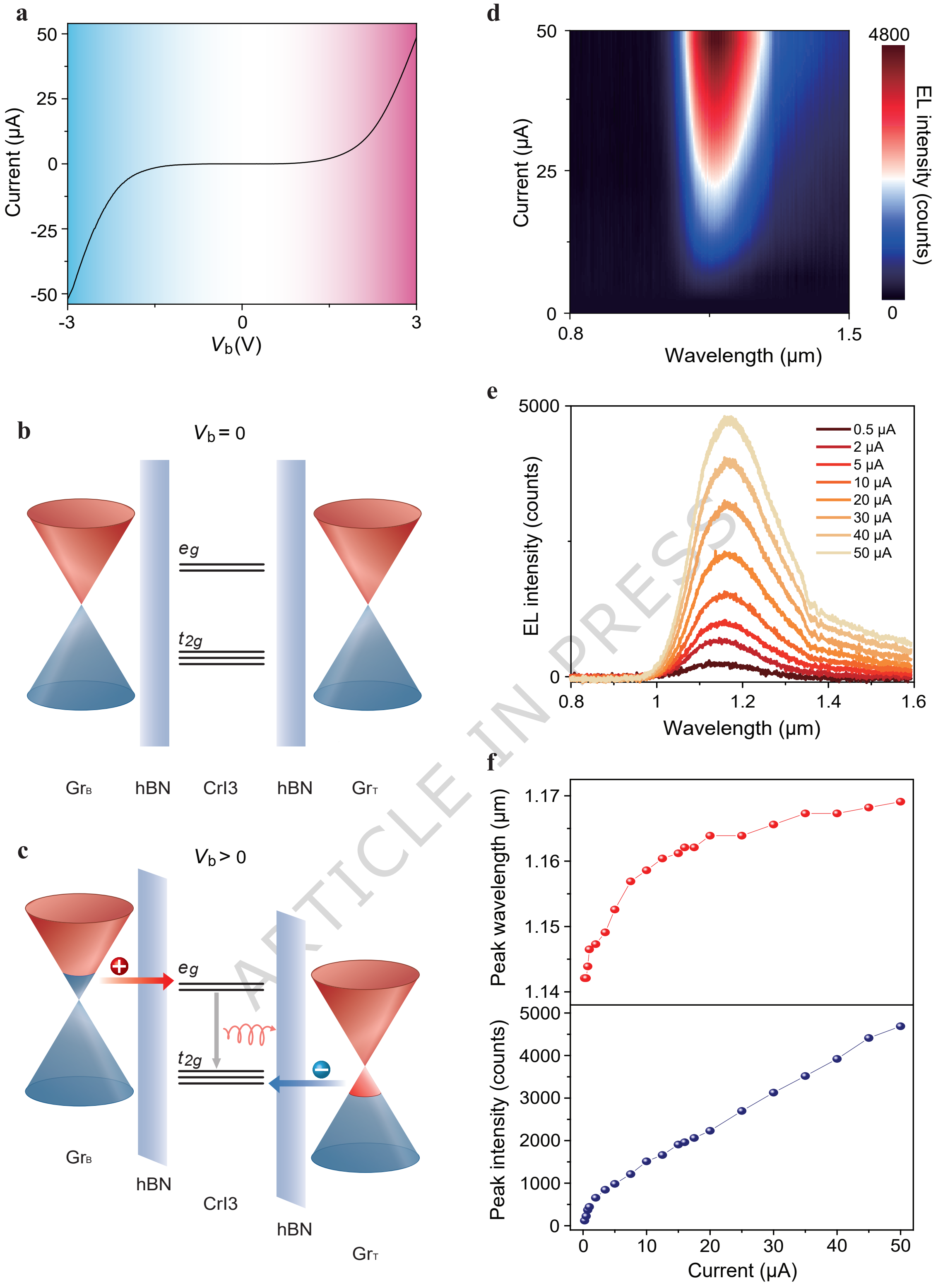
a
50
25
0
-25
-50
Current (μA)
-3
0
3
V_b(V)
b
$V_b = 0$
eg
t_{2g}
Gr$_B$
hBN
CrI3
hBN
Gr$_T$
c
$V_b > 0$
eg
t_{2g}
Gr$_B$
hBN
CrI3
hBN
Gr$_T$
d
50
25
0
Current (μA)
0.8
1.5
Wavelength (μm)
4800
0
EL intensity (counts)
e
5000
0
EL intensity (counts)
0.5 μA
2 μA
5 μA
10 μA
20 μA
30 μA
40 μA
50 μA
0.8
1
1.2
1.4
1.6
Wavelength (μm)
f
1.17
1.16
1.15
1.14
Peak wavelength (μm)
5000
4000
3000
2000
1000
0
Peak intensity (counts)
0
10
20
30
40
50
Current (μA)

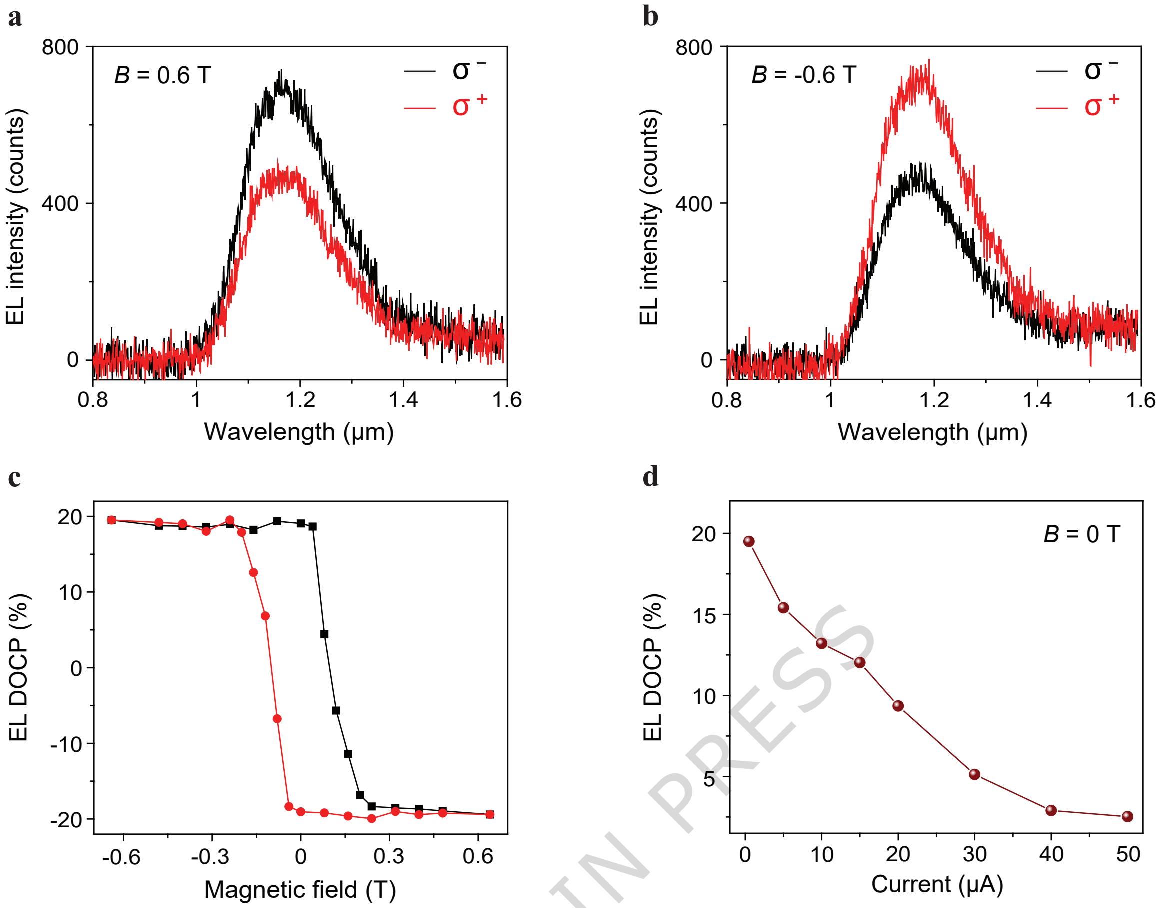
a
B = 0.6 T
σ⁻
σ⁺
EL intensity (counts)
800
400
0
0.8
1
1.2
1.4
1.6
Wavelength (μm)
b
B = -0.6 T
σ⁻
σ⁺
EL intensity (counts)
800
400
0
0.8
1
1.2
1.4
1.6
Wavelength (μm)
c
EL DOCP (%)
20
10
0
-10
-20
-0.6
-0.3
0
0.3
0.6
Magnetic field (T)
d
B = 0 T
EL DOCP (%)
20
15
10
5
0
10
20
30
40
50
Current (μA)